

See discussions, stats, and author profiles for this publication at: <https://www.researchgate.net/publication/303771472>

# Strain based FBG sensor for real-time corrosion rate monitoring in pre-stressed structures

Article in Sensors and Actuators B Chemical · June 2016

DOI: 10.1016/j.snb.2016.05.167

---

CITATIONS

28

READS

547

---

5 authors, including:



Khalil Al Handawi

McGill University

9 PUBLICATIONS 44 CITATIONS

[SEE PROFILE](#)



Nader Vahdati

Khalifa University

63 PUBLICATIONS 544 CITATIONS

[SEE PROFILE](#)



Paul Rostro

Khalifa University

42 PUBLICATIONS 172 CITATIONS

[SEE PROFILE](#)



Lydia Lawand

McGill University

8 PUBLICATIONS 44 CITATIONS

[SEE PROFILE](#)

Some of the authors of this publication are also working on these related projects:



Corrosion flow loop design and build [View project](#)



Aeroelastic model system identification [View project](#)

# Strain based FBG sensor for real-time corrosion rate monitoring in pre-stressed structures

Khalil Al Handawi\*, Nader Vahdati, Paul Rostron, Lydia Lawand, Oleg Shirayev

*The Petroleum Institute, Umm Al Nar, Main Campus, Dept. of Mechanical Engineering, Abu Dhabi, United Arab Emirates*

---

## Abstract

A strain based corrosion sensor for the detection of environmental corrosion of pre-stressed structures was developed and tested on mild steel specimens readily available. Theoretically, a beam shaped specimen under a displacement load exhibits a linear relationship between the strain observed at any point through the thickness of the beam cross-section. This property was exploited to detect thickness changes in pre-stressed mild steel specimens in a double bending configuration under an electrochemically excited corrosion reaction. The reaction was accelerated by supplying a DC current to the cell where the specimens act as anodes of the system, while graphite rods serve as cathodes. The strain was logged using fiber optic Bragg grating technology and conventional electrical strain gages simultaneously. Results show a strong relationship between the corrosion rate observed by back-calculation from supplied current and the time derivative of the measured strain values. Application of this sensor can therefore be extended to a variety of structures under mechanical loading, proving valuable for both its ability to measure corrosion rate in real-time, while maintaining an intrinsically safe nature appropriate by industrial standards.

*Keywords:*

Optical sensors, Fiber Bragg grating technology, Real-time Monitoring, Corrosion rate sensing

---

## 1. Introduction

Oil pipelines commonly encountered in the Oil and Gas industry are used as transfer lines spanning large distances [1]. As part of the industry's efforts in ensuring asset integrity and employee well-being, a Pipeline Integrity Management (**PIM**) program is established at the Abu Dhabi National Oil Company (ADNOC) to assess and mitigate pipeline risks. In order to assess pipeline integrity a multitude of monitoring tools are used [2]. In the United Arab Emirates (UAE), pipelines operate in weather conditions of extreme humidity and heat. As a result, civil structures are frequently attacked by the various mechanisms of corrosion.

The industry is faced with the challenge of inspecting pipelines spanning several kilometers for environmental corrosion due to the severe weather

conditions. This paper aims to address the above problem by using residual stress relief as a mechanism for quantifying corrosion rate.

Oil transfer pipelines are subject to large internal pressures particularly at the crude oil inlet to propel the fluid large distances. Internal pressure gives rise to axisymmetric stress profiles resulting in circumferential (hoop), radial and axial stresses. An attempt at exploiting axisymmetric stress relief for corrosion detection has been made in the past. However, some complexities are pointed out in this paper and a different approach is proposed.

Axisymmetric stresses are similar to residual stresses that may be introduced to structures via machining processes or differential cooling rates that follow. Residual stresses are difficult to quantify unless relieved by removing material from the part and measuring the resulting change in strain. Corrosion being an inherently destructive process, will relieve stored residual stresses over time. The rate of corrosion can be estimated from strain measurement to quantify the severity of corrosion dam-

---

\*Corresponding author. Tel.: +971 501786051  
Email address: khbalhandawi@pi.ac.ae (Khalil Al Handawi)

## Nomenclature

$y$	beam displacement in $y$ -direction	$\lambda_B$	Nominal Bragg wavelength
$x$	Axial coordinate along beam length	$n$	Effective refractive index
$M(x)$	Bending moment	$\Lambda$	Grating spacing/pitch
$E$	Young's modulus	$\Delta\lambda_B$	Shift in Bragg wavelength
$I$	Second moment of the area	$\Delta\Lambda$	Change in grating spacing/pitch
$F$	Beam end-load	$\Delta n$	Change in core refractive index
$L$	Length of beam	$\varepsilon_1$	Normal axial strain to fiber axis
$\alpha$	Arctan of slope of beam fixed end	$\varepsilon_t$	Tangential strain to fiber axis
$\sigma$	Bending stress in beam	$p_{11}$	Pockels' normal photoelastic constant
$c$	Distance to outermost edge from beam neutral axis	$p_{12}$	Pockels' shear photoelastic constant
$\delta$	Thickness of beam	$p_e$	Effective photoelastic contribution
$\varepsilon$	Bending strain of beam	$C_E$	Strain-corrosion scale constant
$t$	Time	$C_I$	Current-corrosion scale constant
$W$	Width	$\frac{d\delta}{dt}$	Percieved corrosion rate by strain measurement
$\nu$	Poisson's ratio	$\left(\frac{d\delta}{dt}\right)_{ref}$	Reference current-set corrosion rate
$\delta_i$	Initial thickness of beam	<b>PIM</b>	Pipeline Integrity Management
$M_l$	Mass loss from beam specimens	<b>FBG</b>	Fiber Bragg Grating
$m$	Atomic mass	<b>UV</b>	Ultra-Violet
$I_c$	Corrosion current	<b>FEM</b>	Finite Element Model
$n_e$	Number of valence electrons	<b>FEA</b>	Finite Element Analysis
$\rho$	Mass density	<b>RI</b>	Refractive Index
$A$	Exposed anodic area	<b>MEMS</b>	Micro Electro-Mechanical System

age.

A number of standardized techniques are used for the quantification of residual stresses in components and structures. Such techniques are classified into destructive, semi-destructive and non-destructive techniques [3].

Among the destructive techniques, the crack compliance method is most widely used with cylindrical geometry [4, 5]. Cuts of varying depths coupled with strain relief measurements using strain gages and a least squares failure model provide a prediction of hoop, axial and radial residual stresses. The deep hole drilling method [6, 7] achieves stress relief by drilling a hole, trepanning it and measuring diameter change to quantify the residual stress field. The technique is validated with four-point bending specimens. Photoelastic strain measurement [8] is coupled with a hole-drilling technique for measuring stresses in a cylindrical tube [9]. Displacement contours are measured via the photoelastic technique and are converted to residual stresses by the theoretical tools developed. Results are then compared against reference electrical strain gage measurements.

The techniques described by Refs. [4–9] employed sophisticated means of measuring strain following stress relief. Such methods are suitable for inspection but not real-time monitoring of structures.

Strain gages used to make the reference measurements are better suited for this purpose but require excitation presenting electrical hazards. Furthermore, strain gages require parallel wiring for each sensing element making system architecture costly and complex. Fiber optic sensors mitigate the previous shortcomings due to their electrical passivity and multiplexing capability [10, 11].

In this paper, a method utilizing Fiber Bragg Grating (**FBG**) sensors is proposed as a monitoring tool. Periodic **FBG** gratings of high and low Refractive Index (**RI**) levels are imprinted in a fiber core by diffracting an Ultra-Violet (**UV**) beam at a controlled diffraction spacing [12]. The phenomenon of photosensitivity alters the reflectance of the core material [13]. **FBG** sensors rely on changes in the **RI** of the gratings or their spacing to shift their spectral response. In context of this paper, strain alters the grating spacing which alters the "Bragg" wavelength of the sensor. The Bragg wavelength is the wavelength of a light pulse at which successive reflections due to scattering from the index variations are completely in phase, reporting maximum reflectance of the pulse at the launch end [14].

Optical sensors have been used in the past featuring two distinct topologies; direct structural monitoring or external environmental corrosion sensors.

A direct pipeline corrosion monitoring system for characterizing the thickness of pipelines and their internal pressure is proposed by Ref. [15]. This system utilizes **FBG** strain sensors arranged in a circumferential configuration around the external surface of the pipeline under inspection. The sensor is experimentally verified and calibrated against internal pressure changes but not for an ongoing corrosion reaction. Furthermore, internal pressure in the pipeline may vary during operation which will also affect the axisymmetric stresses of the pipeline, shadowing stress relief due to pipeline corrosion. Without an internal pressure compensation technique, this method will need further refinement for an accurate corrosion rate measurement.

External environmental corrosion sensors feature a material sample from the structure being monitored. An optical transducer (**FBG** or other types) is coupled to the material sample to identify the environmental or ambient corrosion rate of the parent structure by placing the sensor in its vicinity. The sample is consumable and is usually replaced once completely corroded. Several fiber optic sensors of this configuration have been developed for ship hulls and aircraft [16–18]. Optical **FBGs** have been first used for corrosion detection with this topology using long-period gratings featuring a metal coat which upon its corrosion alters the grating volume and therefore its spacing [19]. Further use of this technique features carbon steel coatings [20].

This paper will address the latter approach due to the limitations of the direct corrosion monitoring topology and the demand for an environmental corrosion sensor for the severe local weather conditions. Furthermore, due to the experimental difficulty of pressurizing and instrumenting a steel pipeline subjected to corrosion, a similar approach to the experimental investigation in Ref. [6] is adopted featuring beam shaped steel specimens under displacement loads placed near the pipeline. The changes in the residual bending stresses due to environmental corrosion are monitored via **FBG** sensors. An experimental study under accelerated corrosion featuring **FBG** sensors and strain gages will serve to provide insight and fundamental knowledge pertaining to the behavior of pre-stressed structures under corrosion damage and an environmental corrosion monitoring solution.

## 2. Modelling of pre-stressed beam specimens subject to corrosion

The experimental procedure described in this paper relies on a beam shaped specimen subjected to constant loading of known magnitude. An analysis of a cantilever beam under displacement loading is used to derive the equations governing the stress and strain levels in the beam. A Finite Element Model (**FEM**) of such a beam is constructed and analyzed under more realistic loading conditions to verify the theory.

### 2.1. Theoretical stress solutions for cantilever beams subject to corrosion thickness loss

Euler-Bernoulli beam theory [21] is used to model the specimen used. Fig. 1 shows the schematic of such a beam with an applied displacement load of known magnitude.

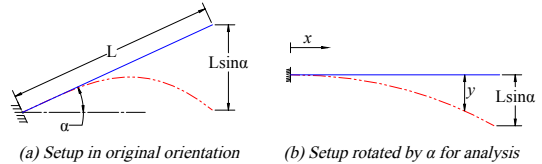


**Fig. 1:** Analytical schematic of specimen under pre-stress in (a) original orientation and (b) horizontal orientation for analysis

The governing equation of Euler-Bernoulli beam deflection is given by:

$$\frac{d^2y}{dx^2} = \frac{M(x)}{EI}, \quad (1)$$

Where  $y$  is the deflection,  $x$  is the distance along the horizontal axis,  $M(x)$  is the bending moment defined as  $FL - Fx$  for cantilever beams with a point load  $F$  applied at the free end,  $E$  is Young's modulus and  $I$  is the second moment of the area for the cross-section of the beam.

Integrating Eq. (1) with the following boundary conditions;  $y(0) = 0$  and  $\frac{dy}{dx}\Big|_{x=0} = 0$ , yields the following:

$$y(x) = \frac{F}{EI} \left( \frac{Lx^2}{2} - \frac{x^3}{6} \right) \quad (2)$$

$$\frac{dy}{dx} = \frac{F}{EI} \left( Lx - \frac{x^2}{2} \right) \quad (3)$$

Setting  $y(L)$  in Eq. (2) to the known displacement of  $L \sin \alpha$ , the required load  $F$  can be calculated as:

$$F = \frac{3EI \sin \alpha}{L^2} \quad (4)$$

175 the bending stress is given by the known formulation:

$$\sigma = \frac{M(x)c}{I} = \frac{F(L-x)c}{I}, \quad (5)$$

180 where  $c$  is the distance from the neutral axis to the outermost fiber which is half the thickness  $\delta$ . Substituting Eq. (4) into Eq. (5) at  $x = L/2$  to obtain the stress in the midsection of the beam yields the following:

$$\sigma = \frac{3E\delta \sin \alpha}{4L} \quad (6)$$

Dividing by Young's modulus as per Hooke's law  $E = \sigma/\varepsilon$  to obtain the strain:

$$\varepsilon = \frac{3\delta \sin \alpha}{4L} \quad (7)$$

185 Eq. (7) provides a relationship for the strain as a function of the thickness  $\delta$ . Taking the time derivative of Eq. (7) and solving for  $d\delta/dt$  yields the following:

$$\frac{d\delta}{dt} = \frac{4L}{3 \sin \alpha} \frac{d\varepsilon}{dt} \quad (8)$$

190 The term  $d\delta/dt$  describes the rate of corrosion. A linear relationship exists between the rate of strain and the corrosion rate, which can be exploited to deduce the rate of corrosion of a certain pre-stressed specimen.

195 An important variable for the design of the pre-stress device is the slope tangent to the specimen at the end of load application. Eq. (3) is solved at  $x = L$  to provide the value of the slope:

$$\left. \frac{dy}{dx} \right|_{x=L} = \frac{3 \sin \alpha}{2} \quad (9)$$

200 Using the previous calculations, beam specimens were constructed from available mild steel stock. The specimens were cut from a 2mm thick sheet of raw material, accurately edge milled to the correct rectangular dimensions and two holes were drilled on both ends for clamping the specimen to the holder. The desired initial thickness was then achieved with a surface grinding machine. Table 1 summarizes material properties and geometric dimensions used in previous calculations.

205 It can be noted that the arctan of the slope in Eq. (9) at the free end of the beam at a location of 52.5 mm is  $3.75^\circ$  ( $1.25^\circ$  for the rotated setup in Fig. 1b). This angle was used to design the holder

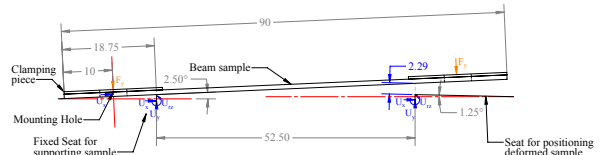
**Table 1:** Material and geometric parameters of machined mild steel specimens

Parameter	Designation	Value
Length (mm)	$L$	52.5
Width (mm)	$W$	10
Slope at fixed end ( $^\circ$ )	$\alpha$	2.5
Young's Modulus (GPa)	$E$	205
Poisson's Ratio	$\nu$	0.33
Initial thickness (mm)	$\delta_i$	0.7, 0.8, 0.9

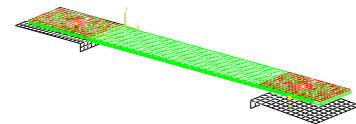
that accommodates the specimens in the proposed configuration.

## 2.2. FEM simulation of double-clamped cantilever beam specimen subject to corrosion thickness loss

Using the calculated geometrical parameters from the theoretical solution, a Finite Element Analysis (**FEA**) was performed to replicate the exact conditions in the experimental apparatus used to apply and maintain pres-stress loads.



(a) Model dimensions and applied boundary conditions



(b) Finite element mesh of the model geometry

**Fig. 2:** Description of finite element model (a) geometry and (b) mesh

Fig. 2 outlines the geometry of the model, the boundary conditions describing the loading conditions and the mesh of the geometry. The analysis was run using commercial finite element software (ABAQUS) in two stages.

The first stage simulates pre-stressing the specimen by applying a clamping pressure on one end followed by a displacement load of 2.89 mm and a clamping pressure applied at the other end to maintain the displacement load. The explicit solver was used to incorporate contact between the specimen and the holders. The results at the mid-section were recorded for each time step and following a period of

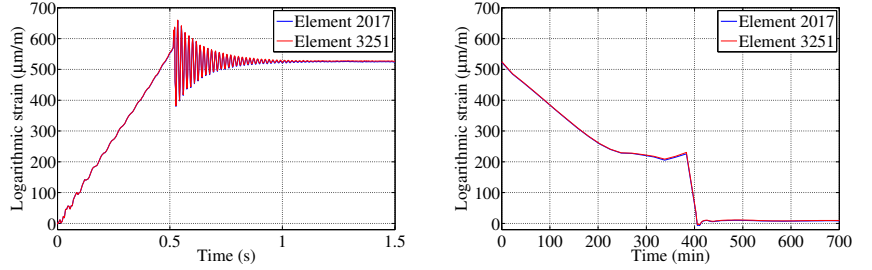


**Fig. 3:** Logarithmic strain FEA result at midsection elements for (a) the pre-stress analysis and (b) the thickness loss analysis

**Note:** Y-axis strain in microstrains ( $\mu\text{m}/\text{m}$ ) is given as dimensionless strain  $\times 10^{-6}$

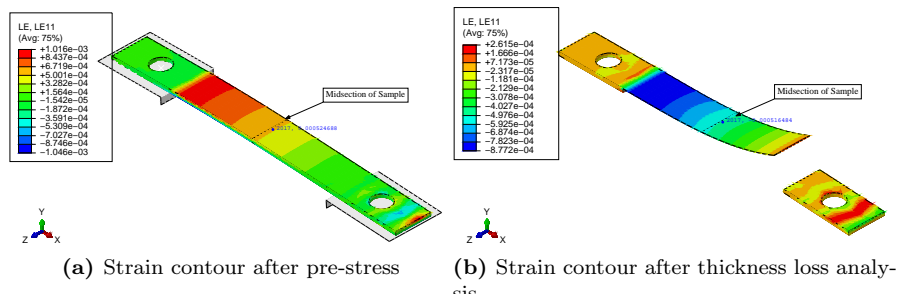


**Fig. 4:** Strain distribution at (a) the end of the pre-stress analysis and (b) relative strain to pre-stressed result after ductile failure due to thickness loss

transience the steady-state logarithmic (true) strain observed at the midsection in Fig. 3a conformed to the value predicted by the theoretical static solution in Sec. 2.1. The strain levels at the center of the specimen were compared with the result of Eq. (7) for various initial thicknesses as depicted in Table 2. This lends credence to the theory being representative of local strains at the mid section where FBG sensors and strain gages are intended to be installed.

**Table 2:** FEA and theoretical (Eq. 7) comparison of mid-section first principle surface strain

Initial thickness $\delta_i$ (mm)	FEA strain ( $\mu\text{m}/\text{m}$ )	Analytical strain ( $\mu\text{m}/\text{m}$ )	% difference
0.9	525.91	560.82	6.22
0.8	485.27	498.50	2.65
0.7	440.40	436.19	0.96

The second stage of the simulation provided insight into the expected experimental results. The orphan mesh from the pre-stress analysis was im-

ported along with the final residual stress field in the specimen. Corrosion was simulated by sequentially removing layers of elements 0.05 mm thick from the analysis starting with the bottom side of the specimen that is under compression. For every layer removed, stress and strain field distributions were re-computed. Strain at the midsection on the top surface was simultaneously monitored and logged. The results, depicted by Fig. 3 show a steady linear decrease in strain as thickness decreases. This is in agreement with the trend described by the strain-thickness relationship Eq. (7).

The strain values reached a plateau towards the final stages of the analysis due to a loss in the stiffness of the specimen, following failure due to a user-defined ductile damage criterion. Contour plots of the strain field at the final state of the specimen at the end of the first and second stages are shown in Fig. 4.

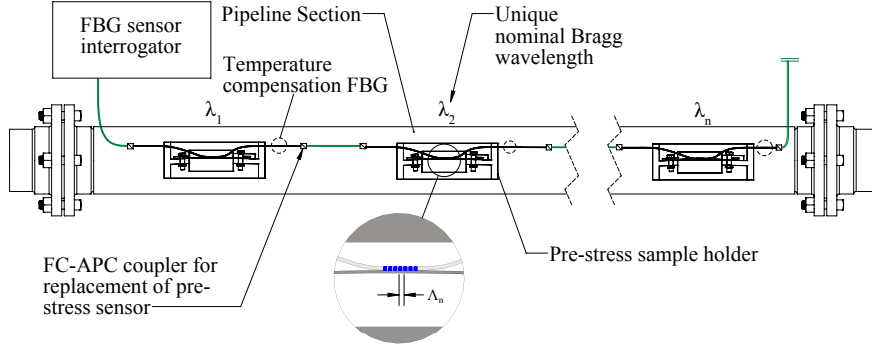


**Fig. 5:** Schematic of proposed pre-stress setup in context of environmental corrosion monitoring for pipelines

### 3. Methodology

This section presents the design methodology used to test the relationship of strain to corrosion rate in beam specimens assumed in theoretical Sec. 2. The experimental procedure described aims to provide an environmental pipeline corrosion monitoring solution that can be used to construct corrosivity maps of a region of interest known for its punishing conditions surrounding the pipeline. Additionally, the experimental results aim to provide a fundamental understanding of the strain sensitivity in the specimens to corrosion in order to provide motivation for researching a direct pipeline corrosion monitoring technique that compensates for internal pressure fluctuations.

In context of an environmental corrosion monitoring system, Fig. 5 shows how the apparatus is intended to be used in a real-pipeline monitoring setting. For a practical implementation, the beam specimens must be constructed from material used in the pipeline's construction. This ensures that the environmental corrosion detected by strain relief of the beam specimens is representative of the pipeline. Additional **FBG** sensors are suggested for temperature compensation by isolating changes in the grating spacing ( $\Lambda$ ) due to thermal expansion from changes caused by mechanical strain relief due to corrosion. Furthermore, each **FBG** occupies a unique spectral bandwidth to allow for sensor multiplexing along a single fiber optic channel [22]. By monitoring the Bragg wavelength of each sensor, information about the corrosivity of its locale can be inferred.

Fig. 6 presents the proposed experimental setup for accelerating corrosion and measuring the resulting strain changes in the steel specimens.

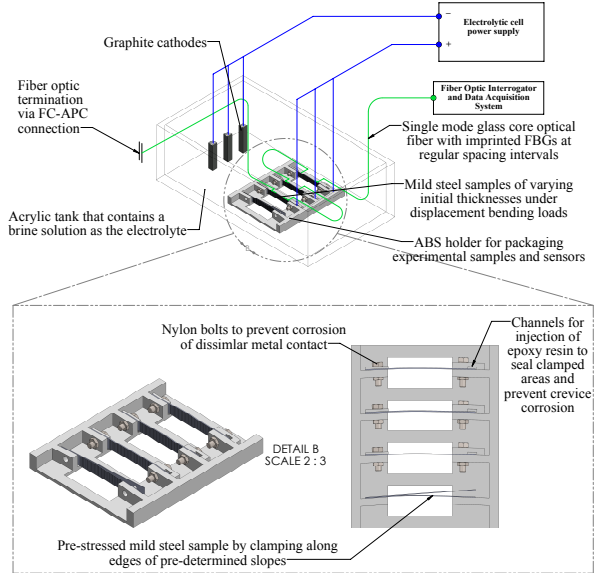
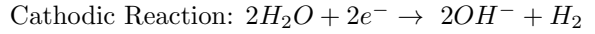
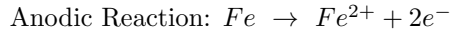


**Fig. 6:** Schematic of proposed electrochemical cell setup for measuring the effect of corrosion on strain of pre-stressed specimens

#### 3.1. Reference corrosion rate measurement scheme

The electric power supply provides a controlled and monitored current to energize the cell and reduce the iron in the steel specimens, accelerating corrosion:



Graphite cathodes are used due to their high electrochemical potential compared to iron in salt water electrolytes and their inert nature causing preferential corrosion of iron. The acrylic tank is used to monitor the progress of the reaction visually and contain the electrolyte solution.

The reference corrosion rate in the experiment is set by the current supplied to the electrolytic cell. Based on Faraday's law governing galvanic cells [23], the amount of mass lost at the anode is given by the following:

$$M_l = \frac{mI_c t}{n_e F}, \quad (10)$$

where  $M_l$  is the mass lost,  $m$  is the molar mass of the metal,  $I_c$  is the current supplied,  $t$  is the time for which current was supplied,  $n_e$  is the number of electrons lost through oxidation of metal and  $F$  is Faraday's constant. By replacing  $M_l = \rho A \delta$ ; where  $A$  is the exposed surface area of the specimen (Length  $\times$  Width) into Eq. (10), taking the time derivative of the thickness  $\delta$ , and solving for  $d\delta/dt$ , the corrosion rate can be seen to be directly proportional to the supplied current  $I_c$ .

$$\left( \frac{d\delta}{dt} \right)_{ref} = \frac{m}{n_e F \rho A} I_c. \quad (11)$$

In the experimental plan, the current supplied to individual specimens is logged by a multi-meter wired in series with the specimens. The current is converted by Eq. (11) into the reference corrosion rate set by the power supply which is used to benchmark the strain sensor results.

### 3.2. Strain measurement scheme

Strain is recorded in two different test setups; one featuring strain **FBG** sensors and the other featuring electrical strain gages. Strain **FBGs** and electrical strain gages are affixed to the mid-section of the steel specimen prior to pre-stressing. Strain **FBGs** imprinted on to a mono-mode SMF-28 fiber are encapsulated by a Santoprene carrier which serves to protect the delicate grating and position the grating accurately over the substrate. An adhesive backing holds the carrier and therefore the grating in place. An injection port (Fig. 7) is provided in the carrier for administering an epoxy mixture (West systems 105 resin with 205 hardener) that will bond the grating to the substrate as it cures over a period of 24 hours. Once cured, the epoxy transfers strain in the substrate to the grating.

Electrical strain gages are also installed in another setup on similar steel specimens and are bonded to the specimen via Loctite 401 due to its ability to proof components against water in the electrolyte.

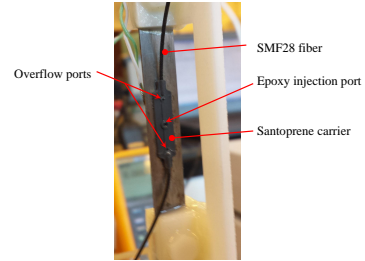


**Fig. 7:** Details of strain **FBG** attachment to steel substrate

Additional Loctite 401 is applied to the surface of the specimens where the strain **FBG** or strain gages are attached limiting corrosion to the bottom surface only allowing the reaction to be easily modeled as was shown in the simulation Sec. 2.2

Strain changes during corrosion of the specimen are detected by **FBG** gratings and strain gages. The fiber optic **FBG** sensor was coupled to an interrogation unit featuring a frequency swept laser pulse source (1510 nm to 1590 nm). The grating reflects or transmits the pulse depending on its Bragg wavelength. Peak reflected powers correspond to the Bragg wavelength of the grating. Shifts in the Bragg wavelength from a nominal value are monitored and post-processed into quantifiable strain. **FBG** theory explains that the Bragg wavelength ( $\lambda_B$ ) is a function of the grating modal/effective index ( $n$ ) and the grating spacing ( $\Lambda$ ) [12]:

$$\lambda_B = 2n\Lambda \quad (12)$$

The above relation in terms of the incremental change in Bragg wavelength is given by the following:

$$\Delta\lambda_B = 2n\Delta\Lambda + 2\Lambda\Delta n \quad (13)$$

The first term of Eq. (13) governs the wavelength shift due to grating spacing ( $\Lambda$ ) while the second term governs the wavelength shift due to a change in the **RI** of the core due to its deformation. Pockels' theory of photoelasticity [24] describes the effect of strain in an isotropic material on the **RI** of the fiber core by pockel's coefficients:

$$\frac{\Delta\lambda_B}{\lambda_B} = \varepsilon_1 - (n^2/2)[p_{11}\varepsilon_t + p_{12}(\varepsilon_1 + \varepsilon_t)] \quad (14)$$

$\varepsilon_1$  is the normal axial strain while  $\varepsilon_t$  gives the tangential strain perpendicular to the fiber axis. Pockels' constants are given by  $p_{11}$  and  $p_{12}$  for an

isotropic material and are obtained from optical material handbooks. Eq. (14) maybe simplified by using the relation:  $\nu = -\varepsilon_t/\varepsilon_1$  for isotropic material obeying Hooke's law:

$$\frac{\Delta\lambda_B}{\lambda_B} = [1 - p_e]\varepsilon_1 \quad (15)$$

where  $p_e = (n^2/2)[p_{12} - \nu(p_{11} + p_{12})]$ . For the specific application used in the experimental work,  $[1 - p_e]$  is given to be 0.796 as per the calibration certificate. Another factor responsible for changing the grating spacing is thermally induced expansion which in the context of this experimental investigation was negligible due to the large thermal capacitance of the electrolyte environment and its sluggish response to external temperature fluctuations.

By substituting Eq. (15) in Eq. (7) the thickness of the specimen in terms of the Bragg wavelength relative change is given as:

$$\delta = \frac{4L}{[1 - p_e]3 \sin \alpha} \frac{\Delta\lambda_B}{\lambda_B} \quad (16)$$

$\lambda_B$  is the nominal Bragg wavelength reported when the specimen is stress-free. Any deviation from the nominal wavelength  $\Delta\lambda_B$  will be logged in time and used to infer the thickness  $\delta$ . The time derivative of  $\delta$  will provide a direct indication of the corrosion or penetration rate. The hardware for the experimental scheme described is now outlined.

#### 415 4. Experimental setup

The experimental setup used to perform the corrosion rate measurements is presented in Fig. 8.

The experiment was run for two different setups outlined in Fig. 8 employing both fiber optic strain FBGs (Micronoptics os3200s strain FBGs interrogated by National Instruments NIPXIe-4844 4 ch. Optical Sensor Interrogator) and electrical strain gages (Omega KFG-10-120-C1-11L3M3R with NI-9237 Full bridge analog input module). The supplied current and potential difference across the cell where logged using Fluke 289 multimeters with IR189USB interface cable. A standard 3.5% by weight  $NaCl$  solution was used as the electrolyte and was prepared from pure  $NaCl$  and distilled water where each constituent was weighed electronically.

The experiments were run until complete failure of all the experimental specimens. High quality soldered joints were used and current levels of 0.5 A

were not exceeded to keep resistive heating to a minimum. The temperature of the electrolyte was monitored by a K-type thermocouple to verify that. The second setup employed a K-type thermocouple probe in direct contact with the steel substrate.

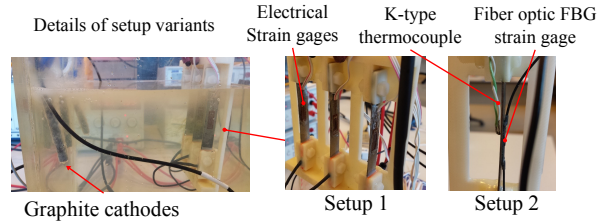


Fig. 8: Experimental setup details of electrolytic corrosion cell and variants of different experimental runs

#### 440 5. Experimental results and discussion

The raw electrical strain gage readings obtained from the first experimental run are shown in Fig. 9a. Three mild steel specimens of different initial thicknesses were tested to study the rate of corrosion on each specimen separately and compare failure times. **FBG** strain sensor data was also obtained and post-processed into strain as shown in Fig. 9b.

The data was filtered by a low-pass filter to reduce noise in strain gage readings and avoid its amplification when finding the time derivative of strain which was then post-processed into corrosion rate.

##### 445 5.1. Data postprocessing for steady state data segment of 1<sup>st</sup> experimental run

A steady decrease in strain was observed as corrosion took place. The 0.9 mm specimen failed before the 0.8 mm specimen, which could be attributed to the lower impedance in the vicinity of the 0.9 mm specimen relative to the 0.8 mm specimen. This is due to the fact that the 0.8 mm specimen was subjected to corrosion products from the two neighboring specimens on either side. In reality, corrosion products would not build up due to much lower corrosion rates encountered in nature. However, regardless of the initial or final state of the specimen, the rate of change of strain is characteristic of the corrosion rate. This can be deduced from results since as established by the theory, strain rate is proportional to corrosion rate. Since all three specimens were under the same corrosion current, their slopes were parallel and equal indicating an equal corrosion rate being sensed by strain relief.

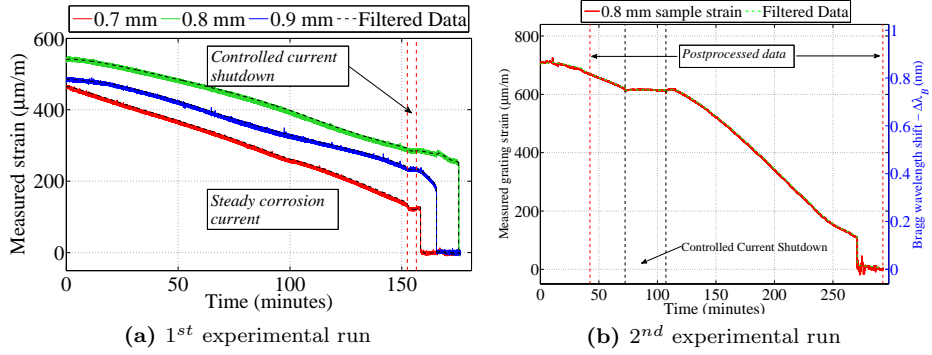


**Fig. 9:** Raw strain gage data obtain from (a) resistance strain gages and (b) fiber optic **FBG** gage

**Note:** Y-axis strain in microstrains ( $\mu\text{m}/\text{m}$ ) is given as dimensionless strain  $\times 10^{-6}$

However, further experimental runs will feature individual specimens tested solely in an electrolytic cell as opposed to testing them in batches. The second experimental run was therefore conducted in this fashion. Furthermore, future tests under natural conditions could be performed in corrosion chambers with potentiostatic techniques [25] used as a corrosion rate reference.

The first part of the data is analyzed to characterize the performance of the proposed sensing technique under a constant current load. First, the time derivative of the filtered strain data ( $d\varepsilon/dt$ ) is obtained from the temporal strain measurements via a finite difference algorithm:

$$\left( \frac{d\varepsilon}{dt} \right)_i = \frac{\varepsilon_{i+1} - \varepsilon_i}{\Delta t} \quad (17)$$

Once the differentiated vector of strain samples ( $d\varepsilon/dt$ ) is obtained, it is transformed to the corrosion rate perceived by the sensing scheme using Eq. (8) as per the procedure in Table 3a.

The measured corrosion current (0.5 A) supplied to the electrolytic cell is transformed to the reference corrosion rate by Eq. (11) as per the procedure in Table 3b. The strain-based corrosion rate ( $\frac{d\delta}{dt}$ ) was benchmarked against the reference corrosion rate ( $\frac{d\delta}{dt}$ )<sub>ref</sub>. The final result for the steady state section of the data recorded in the first run is shown in Fig. 10a.

The corrosion rate predicted using the strain-based method is comparable to the reference current corrosion rate. Minor transience in the strain response to corrosion rate can be noted due to the electrical properties of the electrolytic cell as will be explained now.

### 5.2. Data postprocessing for transient data segment of 1<sup>st</sup> experimental run

The current supply was suddenly switched off at the time interval 152.5 minutes to 156.5 minutes bringing the corrosion rate to zero. This event is illustrated in Fig. 11. As with the steady state data segment from the 1<sup>st</sup> experimental run, the strain and current were transformed using the same procedure and coefficients in Sec. 5.1.

A slow step response is observed due to the capacitive behavior of the electrolytic cell when the current is switched off. Stored charges at the anode slowly traverse the electrolyte, which now acts as a dielectric material causing a capacitive discharge. This indicates a transient response due to current changes in the electrolytic cell. However, since corrosion in a real world environment is a quasi-static phenomenon, steady-state conditions can be assumed for practical implementations.

It was observed that the current fluctuates severely following a failure of the specimen causing erratic changes in the computed corrosion rate that are clouded by the capacitive discharge of the corrosion cell. Consequently, it was decided that the data from that period of time will not be critically analyzed.

### 5.3. Data postprocessing for FBG strain data of 2<sup>nd</sup> experimental run

A second experimental run utilizing an **FBG** sensor on a single specimen was conducted, while closely measuring its temperature via a K-type thermocouple that is pressed against the specimen to ensure temperature is constant and no thermal expansion occurred. The use of thermal paste was

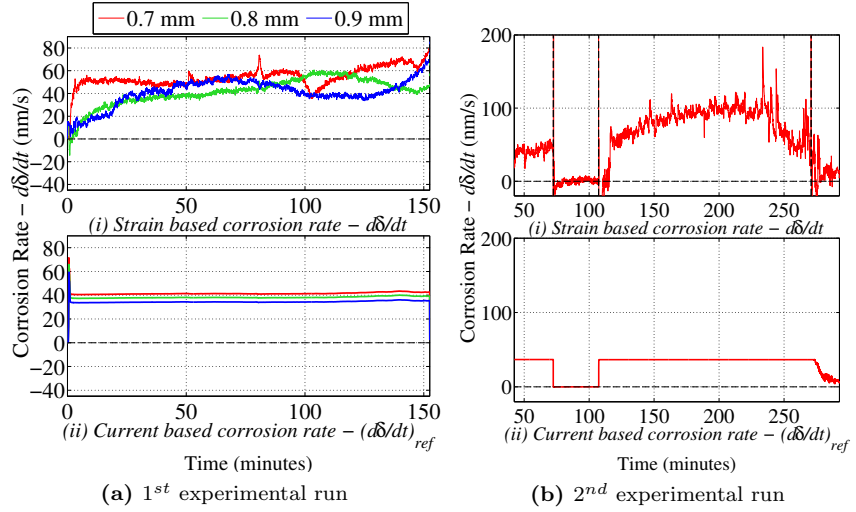


**Fig. 10:** Postprocessed (i) strain based corrosion rate and (ii) current set corrosion rate for (a) the first experimental run and (b) the second experimental run

avoided as to not shield the surface of the specimen from corrosion. The specimen's initial thickness was 0.8 mm and results reported in Fig. 9b show a similar trend to that observed in the first experimental run. The shift in Bragg wavelength was measured in real-time relative to a nominal Bragg wavelength of 1532 nm corresponding to the origin of the second y-axis of Fig. 9b. The wavelength shift from this nominal value is converted to mechanical strain via Eq. (15) where  $[1-p_e]$  is given to be 0.796. The mechanical strain obtained is then operated on in an identical fashion to the strain from the first

experimental run in Secs. 5.2 and 5.1 through Table 3a. Measured supply current of 0.5A was also processed similarly (Table 3b). Similar to the first run, the current was switched off to demonstrate the sensitivity of strain relief measured by the **FBG** sensor to corrosion (minute 72 - minute 107). The Reference corrosion rate for this experimental run is shown in Fig. 10b.

The results in Fig. 10b show comparable corrosion rate values when benchmarked against the reference current-set corrosion rate with a noted increase in the rate of corrosion due to plastic strain

**Table 3:** Corrosion rate calculation from experimental data

Parameter	Designation	Value
<b>(a) Strain based corrosion calculation:</b>		
Length (m)	$L$	$52.5 \times 10^{-3}$
Slope of fixed end ( $^{\circ}$ )	$\alpha$	2.5
Strain rate ( $\mu\text{m}/\text{min}$ )	$\frac{d\varepsilon}{dt}$	from Eq. (17)
Conversion constant	$C_E = \frac{4L}{3\sin\alpha} \times \frac{1}{60} \frac{\text{min}}{\text{s}} \times 1000 \frac{\text{nm}}{\mu\text{m}}$	26.747
Strain based corrosion rate (nm/s)	$\frac{d\delta}{dt} = C_E \times \frac{d\varepsilon}{dt}$	Fig. 10a(i), Fig. 10b(i), Fig. 11(i)
<b>(b) Current based corrosion calculation:</b>		
molar mas of iron (kg/mol)	$m$	$56 \times 10^{-3}$
Number of valence electrons	$n_e$	2
Faraday's constant (C/mol)	$F$	96,485
Density of steel ( $\text{kg}/\text{m}^3$ )	$\rho$	7,850
Anodic area ( $\text{m}^2$ )	$A = W \times L$	$50 \times 10 \times 10^{-6}$
Corrosion current (A)	$I_c$	from multimeter data
Conversion constant	$C_I = \frac{m}{n_e F \rho A} \times 10^9 \frac{\text{nm}}{\text{m}}$	73.936
Current based corrosion rate (nm/s)	$\left(\frac{d\delta}{dt}\right)_{ref} = C_I \times I_c$	Fig. 10a(ii), Fig. 10b(ii), Fig. 11(ii)

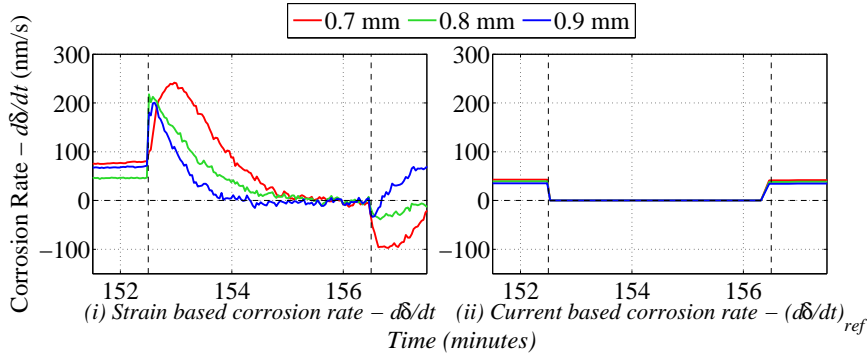


**Fig. 11:** Strain, time derivative of strain and current levels supplied at the time of switching off the current supply

in the specimen. The plastic strain is attributed to the machining processes used to drill mounting holes in the specimen. As a result, future specimens should be annealed prior to testing in order to relieve plastic strains.

The optical method for measuring strain using **FBG** gratings shows promise in its close response to electrical strain gages when comparing the results of the first (employing strain gages) and second experimental runs (employing **FBG** gratings) in Fig. 9. Both strain measurement methods feature a similar response to uniform corrosion with a slope corresponding to the rate of corrosion. Both setups show no strain relief as given by zero slopes when the current to the cell is switched off. The experimental work lends credence to the feasibility of the proposed corrosion measurement scheme using **FBG** gratings and reinforces the arguments made in Sec. 3.

Illustrations of the condition of the specimens at the end of each experimental run can be seen in Fig. 12.

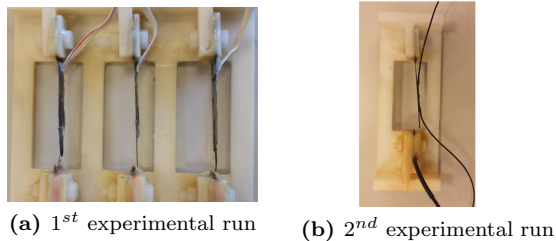


**Fig. 12:** Remains of specimens at the end of (a) first and (b) second experimental runs

## 6. Conclusion of experimental section

Experimental results performed on pre-stressed beam specimens have shown that strain relief measurement due to corrosion provides a good indication of its rate when benchmarked against a reference corrosion rate. This technique can be extended to monitoring environmental corrosion near pipelines and tanks commonly encountered in the oil & gas industry. However, the utilization of the technique's electrical strain gages may prove inappropriate by oil & gas safety standards, in which case fiber optic **FBG** sensors would provide a suitable alternative. The holder and specimen assembly used are proposed to be scaled down to a Micro Electro-Mechanical System (**MEMS**), device which can be placed in the outside environment near the pipeline to report its corrosivity.

Additionally, the technique described in this paper can accurately report corrosion rate in real-time and provide live data about the environmental corrosion rate, unlike the use of "fuse" sensors that only show a changed reading at the time of failure.

Further work on this technique can be carried out on a variety of structures and components. The proposed sensing principle can be applied to oil & gas pipelines by mounting it directly in a circumferential fashion to capture changes in hoop stress. However, an internal pressure compensation scheme is required for reliable pipeline corrosion indication.

## 7. Acknowledgments

The authors are grateful to the Abu Dhabi National Oil Company (ADNOC) and the Abu Dhabi Company for Onshore Oil Operations (ADCO) for funding this research.

- [1] M. S. El-Abbasy, A. Senouci, T. Zayed, F. Mirahadi, L. Parvizsedghy, Artificial neural network models for predicting condition of offshore oil and gas pipelines, *Automation in Construction* 45 (2014) 50–65.
- [2] H. A. Kishaway, A. H. Cabbar, Review of pipeline Integrity management practices, *International Journal of Pressure Vessels and Piping* 87 (2010) 373–380.
- [3] N. S. Rossini, M. Dassisti, K. Y. Benyouounis, A. G. Olabi, Methods of measuring residual stresses in components, *Materials and Design* 35 (2012) 572–588.
- [4] W. Cheng, I. Finnie, Measurement of residual hoop stresses in cylinder using the compliance method, *Journal of Engineering Materials and Technology* 108 (1986) 87–92.
- [5] W. Cheng, I. Finnie, Ö. Vardar, Estimation of axisymmetric residual stresses in a long cylinder, *Journal of Engineering Materials and Technology* 114 (1992) 137–140.
- [6] R. H. Leggatt, D. J. Smith, S. D. Smith, F. Faure, Development and experimental validation of the deep hole method for residual stress measurement, *Journal of Strain Analysis* 31 (1996) 177–186.
- [7] S. Hossain, C. E. Truman, D. J. Smith, Finite element validation of the deep hole drilling method for measuring residual stresses, *International Journal of Pressure Vessels and Piping* 93–94 (2012) 29–41.
- [8] J. T. W. Corby, W. E. Nickola, Residual strain measurement using photoelastic coatings, *Optics and Lasers in Engineering* 27 (1997) 111–123.
- [9] Y. Ma, X. Yao, D. Zhang, Axially symmetrical stresses measurement in the cylindrical tube using DIC with hole-drilling, *Optics and Lasers in Engineering* 66 (2015) 174–180.
- [10] M. Majumder, T. K. Gangopadhyay, A. K. Chakraborty, K. Dasgupta, D. K. Bhattacharya, Fibre Bragg gratings in structural health monitoring—Present status and application, *Sensors and Actuators A* 147 (23) (2008) 150–164.
- [11] Y. J. Rao, Recent progress in applications of in-fibre Bragg grating sensors, *Optics and Lasers in Engineering* 31 (1999) 297–324.
- [12] K. O. Hill, G. Meltz, Fiber bragg grating technology: fundamentals and overview, *Journal of Lightwave Technology* 15 (1997) 1263–1275.
- [13] K. O. Hill, Y. Fujii, D. C. Johnson, , B. S. Kawasaki, Photosensitivity in optical fiber waveguides: Application to reflection filter fabrication, *Applied Physics Letters* 32 (1978) 647–649.
- [14] W. W. Morey, G. Meltz, W. H. Glenn, Fiber optic bragg grating sensors, *Proc. SPIE* 1169 (1990) 98–107.
- [15] L. Ren, Z. Jia, H. Li, G. Song, Design and experimental study on fbg hoop-strain sensor in pipeline monitoring, *Optical Fiber Technology* 20 (2014) 15–23.
- [16] D. Saying, L. Yanbiao, T. Qia, L. Yanan, Q. Zhigang, S. Shizhe, Optical and electrochemical measurements for optical fibre corrosion sensing techniques, *Corrosion Science* 48 (2006) 1746–1756.
- [17] M. Benounis, N. Jaffrezic-Renault, Elaboration of an optical fibre corrosion sensor for aircraft applications, *Sensors and Actuators B* 100 (16) (2004) 1–8.
- [18] A. M. Cardenas-Valencia, R. H. Byrne, M. Calves, L. Langebrake, D. P. Fries, E. T. Steimle, Development of stripped-cladding optical fiber sensors for continuous monitoring II: Referencing method for spectral sensing of environmental corrosion, *Sensors and Actuators B* 122 (2007) 410–418.
- [19] J. A. Greene, M. E. Jones, T. A. Tran, K. A. Murphy, P. M. Schindler, V. Bhatia, R. G. May, D. Sherrer, R. O. Claus, Grating-based optical-fiber-based corrosion sensors, *Proc. SPIE* 2718 (1996) 170–174.
- [20] W. Hu, H. Cai, M. Yang, X. Tong, C. Zhou, W. Chen, FeC-coated fibre Bragg grating sensor for steel corrosion monitoring, *Corrosion Science* 53 (5) (2011) 1933 – 1938.
- [21] O. A. Bauchau, J. I. Craig, *Structural Analysis*, Springer Netherlands, Dordrecht, 2009, Ch. Euler-Bernoulli beam theory, pp. 173–221.
- [22] A. T. Alavie, S. E. Karr, A. Othonos, R. M. Measures, A multiplexed bragg grating fiber laser sensor system, *IEEE Photonics Technology Letters* 5 (9) (1993) 1112–1114.
- [23] Z. Ahmad, *Principles of Corrosion Engineering and Corrosion Control*, Butterworth-Heinemann, Oxford, 2006, Ch. Corrosion Kinetics, pp. 57 – 119.
- [24] T. S. Narasimhamurty, Pockels' phenomenological theory of photoelasticity of crystals, in: *Foundation For Guided Wave Optics*, Hoboken, New Jersey: John Wiley & Sons, 1981, pp. 47–133.
- [25] Electrochemical polarization techniques for corrosion monitoring, in: L. Yang (Ed.), *Techniques for Corrosion Monitoring*, Woodhead Publishing.